Key Points:
- The 410 and 660 km discontinuities beneath the Tanzania Craton (TC) and the Eastern and Western Branches are imaged using receiver functions
- Normal MTZ thickness is found beneath the Western Branch and the TC, implying the absence of significant thermal upwelling from lower mantle
- While the cause of a 30 km MTZ thinning beneath the Eastern Branch remains enigmatic, overall results are inconsistent with active rifting

Supporting Information:
- Supporting Information S1
- Table S1

Correspondence to:
S. S. Gao,
sgao@mst.edu

Receiver Function Imaging of Mantle Transition Zone Discontinuities Beneath the Tanzania Craton and Adjacent Segments of the East African Rift System

Muchen Sun[1,2] [ID], **Kelly H. Liu[2]** [ID], **Xiaofei Fu[1]** [ID], and **Stephen S. Gao[2]** [ID]

[1]College of Earth Science and Research Institute of Unconventional Oil and Gas, Northeast Petroleum University, Daqing, China, [2]Geology and Geophysics Program, Missouri University of Science and Technology, Rolla, MO, USA

Abstract The mantle transition zone (MTZ) discontinuities beneath the Tanzania Craton and the Eastern and Western Branches of the East African Rift System are imaged by stacking over 7,100 receiver functions. The mean thickness of the MTZ beneath the Western Branch and Tanzania Craton is about 252 km, which is comparable to the global average and is inconsistent with the existence of present-day thermal upwelling originating from the lower mantle. In contrast, beneath the Eastern Branch, an up to 30 km thinning of the MTZ is observed and is attributable to upwelling of higher temperature materials from either the upper MTZ or the lower mantle. The observations are in agreement with the hypothesis that rifting in Africa is primarily driven by gradients of gravitational potential energy and lateral variations of basal traction force along zones of significant changes of lithospheric thickness such as the edges of the Tanzania Craton.

1. Introduction

The initiation and development of the East African Rift System (EARS), which is an archetype of continental rifts, remain enigmatic in spite of numerous studies (Burke & Wilson, 1972; Ebinger & Sleep, 1998; Foulger et al., 2013; Koptev et al., 2015; Rychert et al., 2012; Stamps et al., 2014, 2015). One of the frequently involved features in rifting models for the EARS is the African superplume, a low-velocity feature in the lower mantle (Nyblade & Robinson, 1994; Ritsema et al., 1999). Previous seismic tomographic studies have reached con-trasting conclusions about whether superplume materials have reached the upper mantle, and if they have played a significant role in the development of the EARS (Chang et al., 2015; Corchete, 2012; Debayle et al., 2001; Fishwick, 2010; Mulibo & Nyblade, 2013a; O'Donnell et al., 2013; 2016 Priestley et al., 2008; Ritsema et al., 1998).

The debate is particularly intensive for the central part of the EARS, where the African lithosphere is divided into the Nubian and Somalian plates and the Victoria and Rovuma microplates by the Eastern and Western Branches which are separated by the Archean Tanzania Craton (TC) (Figures 1 and S1 in the supporting information) (Chorowicz, 2005). This controversy is most likely caused by the limited vertical resolution of the tomographic techniques and the pervasive use of relative (rather than absolute) travel time residuals (Foulger et al., 2013), as well as the wavefront healing effects of deep and thin (relative to the wavelength) mantle plumes (Montelli et al., 2004).

Petrophysical, geodynamic modeling, and observational studies conducted over the past several decades have demonstrated that the topography of the mantle transition zone (MTZ) discontinuities found ubiqui-tously at the globally averaged depths of approximately 410 km (d410) and 660 km (d660) are functions of MTZ water content and in situ temperature in the vicinity of the discontinuities (Flanagan & Shearer, 1998; Hirose, 2002; Ringwood, 1991; Shearer & Masters, 1992). Specifically, a depression of the d410 indicates a higher than normal temperature due to the positive Clapeyron slope of the olivine-wadsleyite transition, while an uplifted d660 is anticipated for areas with thermal upwelling from the lower mantle, as a result of the negative Clapeyron slope of the ringwoodite to bridgmanite and ferropericlase phase transition (Helffrich, 2000; Ringwood, 1975; Tschauner et al., 2014). If the temperature at the bottom of the MTZ increases from the estimated normal value of approximately 1600°C to higher than 1800°C, the dominant phase transition asso-ciated with the d660 becomes the transition from majorite to perovskite, which has a positive Clapeyron slope
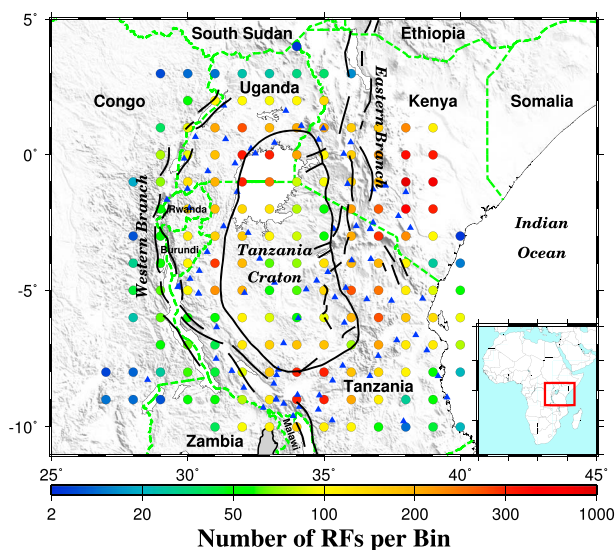
Figure 1. Topographic relief map of the study area showing the center of radius = 1° bins (filled circles), and major tectonic boundaries (solid black lines). The color of the circles represents the number of RFs per bin. The blue triangles are seismic stations used in the study, and the green lines are national boundaries. The red rectangle in the inset map shows the study area.

of +1.0 MPa/K (Hirose, 2002). Anomalously high-water content in the MTZ has similar effects as low temperature, that is, leading to an uplifted d410 and depressed d660 and consequently a thicker than normal MTZ (Litasov et al., 2005; Ohtani et al., 2004).

Several studies of MTZ discontinuities have been conducted in the EARS, frequently with controversial conclusions regarding the thermal state of the MTZ and rifting mechanisms. Owens et al. (2000) and Huerta et al. (2009) imaged the structure of the MTZ beneath the EARS based on the 3-D model of Ritsema et al. (1998) and the 1-D IASP91 model, respectively. Both studies revealed a locally depressed d410 beneath the Eastern Branch and a widely depressed d660 beneath the TC and adjacent areas and suggested the existence of a mantle plume traversing both the d660 and d410 and reaching shallow mantle depths. Mulibo and Nyblade (2013b) corrected the depths of the d410 and d660 by using a 3-D velocity model (Mulibo & Nyblade, 2013a). Their results implied that the superplume induced a thinning of the MTZ beneath a broad area of Eastern Africa, including the Eastern Branch and the central and southern regions of the TC, and advocated for pervasive thermal upwelling of superplume-originated material through the MTZ and its active role in rift development.

Results from some other MTZ studies, however, are inconsistent with the existence of mantle plumes rising from the lower mantle traversing the MTZ. Julia and Nyblade (2013) utilized 2,557 P wave receiver functions from 30 permanent broadband stations in Africa to image the MTZ discontinuities and found no significant thinning of the MTZ beneath the EARS. Tauzin et al. (2008) conducted a global study and found no clear evidence for the thinning of the MTZ beneath the EARS. Beneath the Afar Depression and Ethiopian Plateau, Reed, Gao, et al. (2016) reported that velocity perturbations in the upper mantle are the major factors for an apparent 40–60 km depression of both MTZ discontinuities. Similarly, beneath the nonvolcanic Okavango Rift in Botswana (Yu, Liu, et al., 2015) and the Malawi Rift which is the southward extension of the Western Branch, no significant thinning of the MTZ is observed (Reed, Liu, et al., 2016).

In this study, we utilized an unprecedented volume of high-quality receiver functions (RFs) to image the MTZ discontinuities beneath the TC and the surrounding Western and Eastern Branches, for the purpose of providing additional constraints on the role that the African superplume may play on the initiation and development of the EARS.
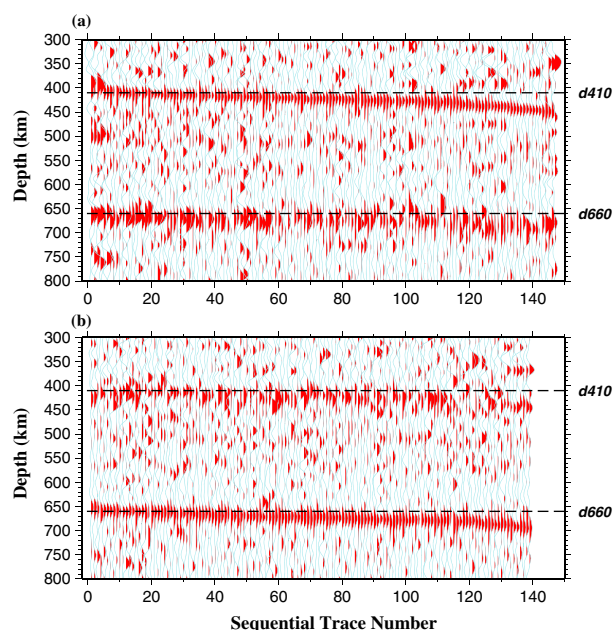
2. Data and Methods

All the broadband seismic data used in the study were obtained from the Incorporated Research Institutions for Seismology (IRIS) Data Management Center (DMC). We requested all the available teleseismic data (epicentral distance range 30–100°) recorded by broadband stations located in the area of −10°N to 5°N and 25°E to 45°E during the recording period from May 1994 to March 2017. The cutoff magnitude (M_c) is determined using the epicentral distance (Δ) and focal depth (D) according to the equation $M_c = 5.2 + (\Delta - 30.0)/(180.0 - 30.0) - D/700.0$ (Liu & Gao, 2010). A four-pole, two-pass band-pass Bessel filter with a frequency range of 0.02–0.2 Hz was applied to the original three-component seismograms. The seismograms with a first-arrival signal-to-noise ratio (SNR) on the vertical component below 4.0 were not used in the study. The SNR is obtained by $\max |A_s|/|\bar{A}_n|$, where $\max |A_s|$ is the maximum absolute amplitude on the vertical seismogram 8 s before and 17 s after the predicted IASP91 arrival time for the first P wave, and $|\bar{A}_n|$ is the mean absolute amplitude in the time window of 10–20 s before the predicted P wave arrival time (Gao & Liu, 2014a, 2014b). The remaining seismograms were converted into radial RFs using the frequency-domain water-level deconvolution procedure with a Gaussian factor of 5.0 (which corresponds to a high-pass corner frequency that is greater than that of the Bessel filter, so that the filtering is solely performed by the latter) and a water level of 0.03 (Ammon, 1991; Clayton & Wiggins, 1976). Before calculating the RFs, we adopted a set of exponential weighting functions to reduce the strong PP arrivals which are found to degenerate the RFs

Figure 2. (a) Results of stacking all available normal moveout-corrected RFs in 1° radius bins with a minimum of six high-quality RFs, plotted with the sequentially increasing depth of the d410. (b) Similar to Figure 2a but for sequentially increasing depth of the d660.

(Gao & Liu, 2014a). A total of 7,139 high-quality RFs from 1,871 events recorded by 87 stations were utilized for this study (Figures 1 and S2).

A non–plane wave assumption approach (Gao & Liu, 2014a) was employed to migrate and stack the P-to-S converted phases generated from the MTZ discontinuities. By considering the difference in ray parameters between the direct P wave and the converted S wave, this approach can more accurately estimate the discontinuity depths and lead to sharper discontinuity images than approaches assuming a plane wavefront. Using the 1-D IASP91 Earth model (Kennett & Engdahl, 1991), the geographic coordinates of the ray-piercing point for each of the RFs were computed at the middle of the MTZ (535 km depth). The moveout-corrected RFs within 1° radius circular bins, which are one geographic degree apart from the neighboring bins (Figure 1), were then stacked to form a depth series for each of the bins. Results from bins with less than six RFs are not used. A bootstrap resampling procedure with 50 resampling iterations (Efron & Tibshirani, 1986; Liu et al., 2003) was used to compute the mean and standard deviation of the MTZ discontinuity depths and MTZ thickness for each bin. Detailed description of the migration and stacking procedures and specific data processing parameters can be found in Gao and Liu (2014a, 2014b).
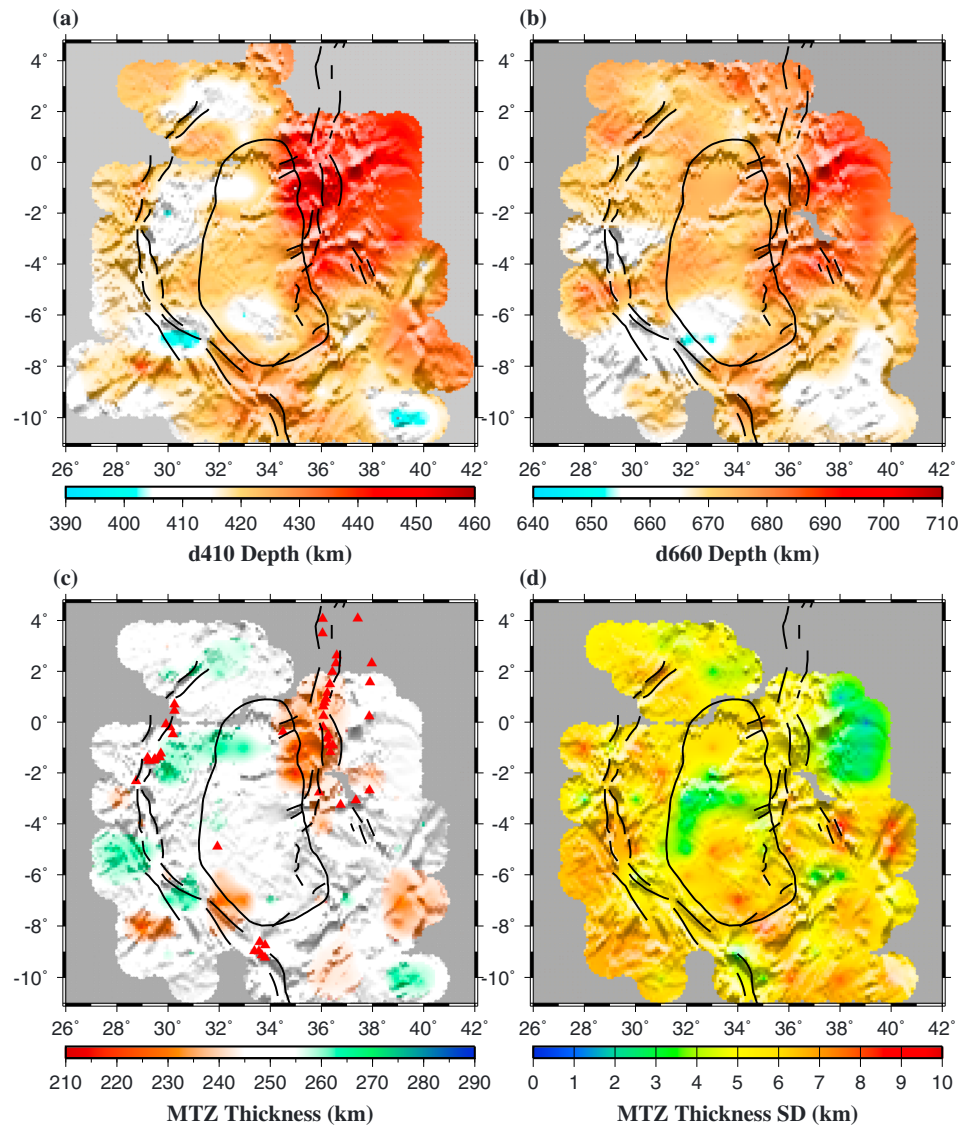
3. Results

For each of the stacked traces, the optimal depth of a MTZ discontinuity is determined using the following steps. First, the depth corresponding to the maximum stacking amplitude in a fixed depth range (380–440 km for the d410 and 650–710 km for the d660) is automatically determined and marked on the trace. Second, the automatically determined depth is visually verified to reject the ones with ambiguous and weak arrivals that are significantly different from neighboring bins. Third, for a small fraction of the traces, the search range is adjusted so that the picked depth is consistent with neighboring bins. A total of 162 bins with clearly observable d410 or d660 peaks were obtained (Figure 2), among which 147, 139, and 124 have reliable peaks for the d410, d660, and both, respectively. Profiles of the resulting depth series along all the 14 latitudinal lines (from 10°S to 3°N with a 1° increment), together with the mean depths and the error bar, are shown in Figure S3, and all the observed depths of the discontinuity arrivals and the MTZ thicknesses are listed in Table S1.

The observations (Figure S1) were fitted with a continuous curvature surface gridding algorithm (Smith & Wessel, 1990) (Figure 3) with a tension factor of 0.5, in order to generate spatially continuous images for the observed depths and MTZ thicknesses. The standard deviation of the resultant MTZ thickness is less than 6 km for the majority of the study area (Figure 3d). The mean apparent depths of the d410 and d660 over the region are 423 ± 12 km and 672 ± 9 km, respectively, and the vast majority of the depths exceed the global averages in the IASP91 Earth model of 410 and 660 km, respectively. The apparent depths of both the d410 and d660 increase systematically toward the northeast part of the study area (Figure 3). The resulting apparent depths of the d410 range from about 390 km beneath the southeastern part of Tanzania to a maximum value of 460 km at the northeastern corner of the study area (Figure 3a). A trend similar to the d410 is observed for the apparent depths of the d660 (Figure 3b).

4. Discussion

The depths of the MTZ discontinuities are calculated under the 1-D IASP91 Earth model, and thus, the depths are apparent rather than true depths. The true depths can only be achieved when absolute (rather than relative to the mean values of a study area) velocity anomalies of both the P and S waves are available for the entire crust, upper mantle, and MTZ (e.g., Gao & Liu, 2014b, for the contiguous United States). Due to the discrepancies in previous seismic tomographic studies, as well as the fact that the vast majority of the studies only reported relative P or S wave (but not both) velocity anomalies for the shallow upper mantle (e.g., Adams et al., 2012; Fishwick, 2010; Pasyanos & Nyblade, 2007; Priestley et al., 2008; Slack & Davis, 1994), such corrections using results from any of the existing tomographic studies would not lead to trustful results.

Figure 3. (a) Spatial distribution of resulting *d*410 apparent depths. (b) Same as Figure 3a but for the *d*660. (c) MTZ thickness measurements. Red triangles represent Cenozoic volcanoes. (d) Standard deviation (SD) of the MTZ thickness measurements.

Therefore, in the following we utilize the observed apparent discontinuity depths to infer velocity, thermal, and water content anomalies.

As discussed in various previous studies, three factors have been recognized to affect the apparent depths of the MTZ discontinuities (see Mohamed et al., 2014, for a more detailed discussion). The first factor is velocity anomalies in the upper mantle, that is, above the *d*410 associated with temperature, partial melting, and compositional heterogeneities. The presence of low and high-velocity anomalies in the upper mantle causes simultaneous apparent depressions and uplifts of both the *d*410 and *d*660, respectively, leading to positively correlated apparent *d*410 and *d*660 depths, as exemplified by the spatial similarities between the *d*410 and *d*660 depths shown in Figures 3a and 3b (correlation coefficient = 0.54). Velocity anomalies in the MTZ can lead to apparent undulations of the *d*660 but not the *d*410 and thus reduce the correlation coefficient. The second factor is the temperature anomalies near the *d*410 and *d*660, which are related to velocity anomalies by a scaling factor of $dV_p/dT = -4.8 \times 10^{-4}$ km s^{-1} °C^{-1} (Deal et al., 1999). For example, assuming a Clapeyron slope of +2.9 MPa/K (Bina & Helffrich, 1994) for the *d*410 and −1.3 MPa/K (Fei et al., 2004) for the *d*660, a 300°C temperature increase around the *d*410 and *d*660 corresponds to a 25 km depression of the *d*410

and a 11 km uplift of the $d660$ for an assumed V_s and V_p relative anomaly ratio ($dln(V_s)/dln(V_p)$) of 1.8 (Gao & Liu, 2014b; Mohamed et al., 2014). Note that because the observed depth undulations are relative to the globally averaged values, for a given depth, the temperature anomalies derived from such undulations are relative to the globally averaged temperature at the same depth. The third factor is the presence of the hydrous materials in the MTZ, which depresses the $d660$ and uplifts the $d410$ (Ohtani et al., 2004).

4.1. Normal MTZ Thicknesses Beneath the TC and Western Branch

Beneath the TC, an ~10 km depression for both the $d410$ (420 ± 7 km) and $d660$ (672 ± 7 km) and a close-to-normal MTZ thickness are observed (Figure 3). The simplest explanation for the observations is a low-velocity upper mantle with a mean V_p anomaly of −0.86%, which is calculated based on Gao and Liu (2014a) using a $dln(V_s)/dln(V_p)$ value of 1.8, a value that is between that suggested for the stable central United States and the tectonically active western United States (Gao & Liu, 2014b; Schmandt & Humphreys, 2010). Additionally, both the weak deepening of the $d410$ and the normal thickness of the MTZ suggest negligible effect of temperature on the MTZ (Deuss, 2007; Tauzin et al., 2008). Reed, Gao, et al. (2016) quantitatively discussed the possibility of the existence of a mantle plume rising from the lower mantle beneath an area with a normal MTZ thickness and suggested that a mantle plume only exists under a specific combination of temperature, hydrous materials, and velocity anomalies. However, this specific combination would be difficult to exist everywhere beneath the entire TC. Therefore, we propose a nonplume model with lateral velocity variation in the upper mantle beneath the TC to explain the apparently depressed MTZ discontinuities with a normal MTZ thickness.

The mean MTZ thickness (252 ± 12 km) and the apparent discontinuity depths beneath the Western Branch are comparable to those of the TC. Those observations are consistent with the previously observed similarity in lithospheric thickness between the two areas (Chesley et al., 1999; Vauchez et al., 2005) and imply the absence of both significant thinning of the mantle lithosphere (Davies, 1994; Rychert et al., 2012) and thermal upwelling of lower mantle materials beneath the Western Branch, favoring a passive rifting mechanism for this section of the EARS.

4.2. Anomalously Thin MTZ Beneath the Eastern Branch

The most prominent feature in the study area is an up to 30 km apparent thinning of the MTZ beneath the Eastern Branch. This thinning is associated with a 50 km apparent depression of the $d410$ and a 20 km depression of the $d660$ (Figure 3). Since the depressed $d410$ and the thinned MTZ can be interpreted as a result of thermally perturbed structure in the upper mantle as well as in the MTZ, two models with and without a thermal upwelling from the lower mantle ("plume and nonplume models") are discussed in the following in order to quantitatively interpret the observed results.

4.2.1. Plume Model

The existence of an active mantle plume beneath the Eastern Branch (Figure S4a) has been proposed based on seismic tomography (Mulibo & Nyblade, 2013a), MTZ topography studies (Huerta et al., 2009; Mulibo & Nyblade, 2013b), geodynamic modeling (Koptev et al., 2015), and geochemical studies (Roberts et al., 2012). In order to produce the observed ~50 km depression of the $d410$, a −1.8% mean V_p and associated high-temperature anomalies in the upper mantle are required. The total depression of 50 km would include a 22 km apparent depression due to the low-velocity upper mantle, and an additional 28 km true depression from the 340°C temperature increase corresponding to the low-velocity anomaly (estimated using a Clapeyron slope of +2.9 MPa/K; Figure 4a). Similarly, the downward extension of the low-velocity zone into the lower mantle would produce a 35 km apparent depression of the $d660$, and a 12 km true uplift of $d660$ (calculated using a Clapeyron slope of −1.3 MPa/K (Fei et al., 2004)), leading to a 23 km net depression of the $d660$. Therefore, the plume model would produce a net 27 km thinning of the MTZ, which is similar to the observed MTZ thickness beneath the Eastern Branch (Figures 3c and 4a).

One potential problem with the plume model is that the low MTZ velocities associated with the plume may correspond to an anomalously high-temperature environment in the vicinity of the $d660$, in which the dominant phase transition is majorite (rather than ringwoodite) to perovskite. Specifically, the normal temperature at the bottom of the MTZ is estimated to be about 1600°C (Ito & Katsura, 1989), while the plume model (Figure 4a) requires a 340°C thermal anomaly at the base of the MTZ, leading to a temperature as high as 1940°C. This required temperature is higher than the 1800°C temperature above which the dominant phase transition becomes majorite to perovskite, which has a positive Clapeyron slope of +1.0 MPa/K (Irifune et al., 1996, Hirose, 2002, Hirose et al., 2001). Applying a +1.0 MPa/K Clapeyron slope for the transition, the $d660$
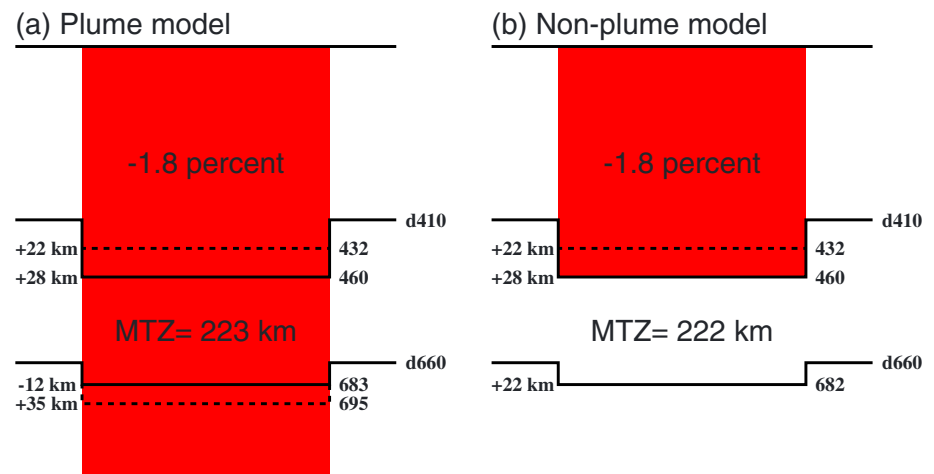
Figure 4. Schematic models to explain the observed depressions of the MTZ discontinuities beneath the Eastern Branch. (a) The plume model, in which a thermal plume with a velocity anomaly of −1.8% and a corresponding thermal anomaly of 340°C rises from the lower mantle. (b) The nonplume model, in which a velocity anomaly exists in the upper mantle as well as the uppermost MTZ. The dashed lines represent the apparent depths of the discontinuities due to the presence of the low velocities, and the solid lines are the final depths. The models produce a 27–28 km thinning of the MTZ.

would depress about 9 km corresponding to the temperature increase. Together with the 35 km apparent depression of the d660 due to the low-velocity upper mantle and MTZ, the d660 would depress about 44 km in total. Because the d410 has a 50 km depression due to both the velocity and thermal effects, the amount of MTZ thinning under the plume model is about 6 km, which is significantly smaller than the observed ∼30 km. It should be noted that those estimates are based on a number of experimentally determined quantities with large uncertainties and variably limiting temperature-pressure conditions, including the velocity and temperature anomaly scaling factor, the $dln(V_s)/dln(V_p)$ value, and the Clapeyron slopes (see Tauzin & Ricard, 2014, for some of the reported values). The existence of partial melts in the upper mantle and the MTZ can also affect the estimated depths. The required temperature anomaly to produce the apparent depression of the discontinuities would reduce if partial melt exists in the upper mantle and MTZ. If a certain amount of melt is present, the temperature in the vicinity of the d660 could be lower than 1800°C, so that the phase transition across the d660 would be from ringwoodite (rather than majorite) to perovskite. Therefore, the existence of a thermal upwelling from the lower mantle cannot be confidently ruled out solely based on those arguments.

4.2.2. Nonplume Model

In this model (Figure S4b), a low-velocity zone with a V_p anomaly of −1.8% reaches the d410 and only extends to the uppermost MTZ (Figure 4b). The low velocities result in an apparent depression of 22 km for both the d410 and d660. In addition, the high temperature associated with the low velocities leads to an additional 28 km depression of the d410, resulting in a 28 km thinning of the MTZ which is comparable to the observed value beneath the Eastern Branch.

Relative to the plume model, the nonplume model is simpler and can more easily explain the spatial correspondence between the surface expression of the rift and the thinned MTZ. However, the cause of the high-temperature anomaly associated with the observed depression of the d410 remains problematic. Upwelling of higher temperature material from the upper MTZ to the upper mantle can certainly increase mantle temperature in the vicinity of the d410, but it is difficult for this process to produce such a high-temperature anomaly. Additionally, this process requires that the MTZ be a thermal boundary layer from which a thermal plume originates, a hypothesis that is inconsistent with geodynamic modeling results (e.g., Schubert et al., 1995).

4.3. Implications on Rifting Mechanisms

The above discussions suggest that ambiguities still remain regarding the existence or absence of thermal upwelling from the lower mantle beneath the northern part of the Eastern Branch, and thus, additional studies are needed in order to resolve this critical issue. However, as detailed below, such uncertainty plays an insignificant role when rifting mechanisms are discussed in light of the new MTZ discontinuity measurements presented in this study.

The possible existence of a thermal upwelling from the lower mantle (under the plume model) beneath the northern part of the Eastern Branch seems to be consistent with the active rifting model. However, a lack of such upwelling in the rest of the Eastern Branch and the entire Western Branch makes such a rifting mechanism unlikely for the Eastern and Western Branches. The absence of significant thermal upwelling from the lower mantle beneath other segments of the EARS has also been inferred for the Afar Depression (Reed, Gao, et al., 2016), the Malawi Rift of the EARS (Reed, Liu, et al., 2016), and the Okavango Rift (Yu, Liu, et al., 2015) and is suggested by geodynamic modeling (Quere & Forte, 2006; Stamps et al., 2014; 2015).

The observations presented in the study are consistent with the hypothesis that rifting in East Africa is driven by gradients of gravitational potential energy probably originating from the African superplume (Lithgow-Bertelloni & Silver, 1998; Moucha & Forte, 2011; Stamps et al., 2014, 2015), and by lateral variations of horizontal basal traction forces applied to the lithosphere in areas with sudden changes of thickness. The latter has recently been exemplified in the EARS by a number of shear wave splitting investigations (Gao & Liu, 2016; Reed et al., 2017; Yu, Gao, et al., 2015). The significant difference in lithospheric thickness (e.g., Ritsema et al., 1998) between the TC and the surrounding rift segments makes the edges of the TC ideal locations for rift development.

5. Conclusions

We have imaged mantle transition zone discontinuities beneath the TC and the surrounding Eastern and Western Branches of the EARS. A parallel 10 km depression of the apparent depths of MTZ discontinuities and normal MTZ thickness reveal a −0.86% mean upper mantle V_p anomaly, and a lack of significant thermal anomaly in the MTZ beneath most of the Tanzania Craton and the Western Branch. In contrast, a 30 km thinning of the MTZ is found beneath the Eastern Branch associated with a 50 km apparent depression of the $d410$ and a 20 km depression of the $d660$. Quantitative analyses of the effects of velocity and thermal anomalies on the observed discontinuity depths suggest that the most plausible and simplest explanation of the observed apparent depressions and the MTZ thinning is a low-velocity zone with a V_p anomaly of −1.8% extending from the surface to the uppermost MTZ. Those observations may suggest the present-day existence of thermal upwelling from either the lower mantle or the uppermost MTZ beneath the northern part of the Eastern Branch and is comparable with the hypothesis that gradients of gravitational potential energy from the African superplume and lateral variations of basal traction force applied to areas with significant changes of lithospheric thickness are probably responsible for rift development in East Africa.

References

Adams, A., Nyblade, A. A., & Weeraratne, D. (2012). Upper mantle shear wave velocity structure beneath the East African plateau: Evidence for a deep, plateauwide low velocity anomaly. *Geophysical Journal International*, *189*(1), 123–142. https://doi.org/10.1111/j.1365-246X.2012.05373.x

Ammon, C. J. (1991). The isolation of receiver effects from teleseismic *P*-waveforms. *Bulletin of the Seismological Society of America*, *81*(6), 2504–2510.

Bina, C. R., & Helffrich, G. (1994). Phase transition Clapeyron slopes and transition zone seismic discontinuity topography. *Journal of Geophysical Research*, *99*(B8), 15,853–15,860. https://doi.org/10.1029/94JB00462

Burke, K., & Wilson, J. T. (1972). Is the African plate stationary? *Nature*, *239*(5372), 387–390. https://doi.org/10.1038/239387b0

Chang, S. J., Ferreira, A. M., Ritsema, J., van Heijst, H. J., & Woodhouse, J. H. (2015). Joint inversion for global isotropic and radially anisotropic mantle structure including crustal thickness perturbations. *Journal of Geophysical Research: Solid Earth*, *120*, 4278–4300. https://doi.org/10.1002/2014JB011824

Chesley, J. T., Rudnick, R. L., & Lee, C.-T. (1999). Re-Os systematics of mantle xenoliths from the East African Rift: Age, structure, and history of the Tanzanian craton. *Geochimica et Cosmochimica Acta*, *63*(7), 1203–1217. https://doi.org/10.1016/S0016-7037(99)00004-6

Chorowicz, J. (2005). The east African rift system. *Journal of African Earth Sciences*, *43*(1), 379–410. https://doi.org/10.1016/j.jafrearsci.2005.07.019

Clayton, R. W., & Wiggins, R. A. (1976). Source shape estimation and deconvolution of teleseismic bodywaves. *Geophysical Journal International*, *47*(1), 151–177. https://doi.org/10.1111/j.1365-246X.1976.tb01267X

Corchete, V. (2012). Shear-wave velocity structure of South America from Rayleigh-wave analysis. *Terra Nova*, *24*(2), 87–104. https://doi.org/10.1111/j.1365-3121.2011.01042X

Davies, G. F. (1994). Thermomechanical erosion of the lithosphere by mantle plumes. *Journal of Geophysical Research*, *99*(B8), 15709–15722. https://doi.org/10.1029/94JB00119

Deal, M. M., Nolet, G., & van der Hilst, R. D. (1999). Slab temperature and thickness from seismic tomography: 1. Method and application to Tonga. *Journal of Geophysical Research*, *104*(B12), 28,789–28,802. https://doi.org/10.1029/1999JB900255

Debayle, E., Leveque, J.-J., & Cara, M. (2001). Seismic evidence for a deeply rooted low-velocity anomaly in the upper mantle beneath the northeastern Afro/Arabian continent. *Earth and Planetary Science Letters*, *193*, 423–436. https://doi.org/10.1016/S0012-821X(01)00509-X

Deuss, A. (2007). Seismic observations of transition zone discontinuities beneath hotspot locations. In G. R. Foulger & D. M. Jurdy (Eds.), *Plates, Plumes, and Planetary Processes* (Vol. 430, pp. 121–136). Boulder, CO: Geological Society of America. https://doi.org/10.1130/2007.2430(07)

Ebinger, C. J., & Sleep, N. H. (1998). Cenozoic magmatism throughout east Africa resulting from impact of a single plume. *Nature*, *395*(6704), 788–791. https://doi.org/10.1038/27417

Efron, B., & Tibshirani, R. (1986). Bootstrap methods for standard errors, confidence intervals, and other measures of statistical accuracy. *Statistical Science*, *1*(1), 54–75. https://doi.org/10.1214/ss/1177013815

Fei, Y., Van Orman, J., Li, J., van Westrenen, W., Sanloup, C., Minarik, W., . . . Funakoshi, K. (2004). Experimentally determined postspinel transformation boundary in Mg_2SiO_4 using MgO as an internal pressure standard and its geophysical implications. *Journal of Geophysical Research*, *109*, B02305. https://doi.org/10.1029/2003JB002562

Fishwick, S. (2010). Surface wave tomography: Imaging of the lithosphere-asthenosphere boundary beneath central and southern Africa? *Lithos*, *120*(1), 63–73. https://doi.org/10.1016/j.lithos.2010.05.011

Flanagan, M. P., & Shearer, P. M. (1998). Global mapping of topography on transition zone velocity discontinuities by stacking SS precursors. *Journal of Geophysical Research*, *103*(B2), 2673–2692. https://doi.org/10.1029/97JB03212

Foulger, G. R., Panza, G. F., Artemieva, I. M., Bastow, I. D., Cammarano, F., Evans, J. R., . . . Yanovskaya, T. B. (2013). Caveats on tomographic images. *Terra Nova*, *25*(4), 259–281. https://doi.org/10.1111/ter.12041

Gao, S. S., & Liu, K. H. (2014a). Imaging mantle discontinuities using multiply-reflected *P*-to-*S* conversions. *Earth and Planetary Science Letters*, *402*, 99–106. https://doi.org/10.1016/j.epsl.2013.08.025

Gao, S. S., & Liu, K. H. (2014b). Mantle transition zone discontinuities beneath the contiguous United States. *Journal of Geophysical Research: Solid Earth*, *119*, 6452–6468. https://doi.org/10.1002/2014JB011253

Gao, S. S., & Liu, K. H. (2016). Rifting initiation through lateral variations of lithospheric basal stress beneath preexisting zones of weakness (Paper No. 229-1). Denver, CO: Geological Society of America Annual Meeting.

Helffrich, G. (2000). Topography of the transition zone seismic discontinuities. *Reviews of Geophysics*, *38*(1), 141–158. https://doi.org/10.1029/1999RG000060

Hirose, K. (2002). Phase transitions in pyrolitic mantle around 670-km depth: Implications for upwelling of plumes from the lower mantle. *Journal of Geophysical Research*, *107*(B4), 2078. https://doi.org/10.1029/2001JB000597

Hirose, K., Fei, Y., Ono, S., Yagi, T., & Funakoshi, K. (2001). In situ measurements of the phase transition boundary in $Mg_3Al_2Si_3O_{12}$: Implications for the nature of the seismic discontinuities in the Earth's mantle. *Earth and Planetary Science Letters*, *184*(3), 567–573. https://doi.org/10.1016/S0012-821X(00)00354-X

Huerta, A. D., Nyblade, A. A., & Reusch, A. M. (2009). Mantle transition zone structure beneath Kenya and Tanzania: More evidence for a deep-seated thermal upwelling in the mantle. *Geophysical Journal International*, *177*(3), 1249–1255. https://doi.org/10.1111/j.1365-246X.2009.04092.x

Irifune, T., Koizumi, T., & Ando, J. (1996). An experimental study of the garnet-perovskite transformation in the system $MgSiO_3$-$Mg_3Al_2Si_3O_{12}$. *Physics of the Earth and Planetary Interiors*, *96*(2–3), 147–157. https://doi.org/10.1016/0031-9201(96)03147-0

Ito, E., & Katsura, T. (1989). A temperature profile of the mantle transition zone. *Geophysical Research Letters*, *16*(5), 425–428. https://doi.org/10.1029/GL016i005p00425

Julia, J., & Nyblade, A. A. (2013). Probing the upper mantle transition zone under Africa with *P520s* conversions: Implications for temperature and composition. *Earth and Planetary Science Letters*, *368*, 151–162. https://doi.org/10.1016/j.epsl.2013.02.021

Kennett, B. L., & Engdahl, E. R. (1991). Traveltimes for global earthquake location and phase identification. *Geophysical Journal International*, *105*(2), 429–465. https://doi.org/10.1111/j.1365-246X.1991.tb06724.X

Koptev, A., Calais, E., Burov, E., Leroy, S., & Gerya, T. (2015). Dual continental rift systems generated by plume-lithosphere interaction. *Nature Geoscience*, *8*(5), 388–392. https://doi.org/10.1038/ngeo2401

Litasov, K. D., Ohtani, E., Sano, A., Suzuki, A., & Funakoshi, K. (2005). Wet subduction versus cold subduction. *Geophysical Research Letters*, *32*, L13312. https://doi.org/10.1029/2005GL022921

Lithgow-Bertelloni, C., & Silver, P. G. (1998). Dynamic topography, plate driving forces and the African superswell. *Nature*, *395*(6699), 269–272. https://doi.org/10.1038/26212

Liu, K. H., & Gao, S. S. (2010). Spatial variations of crustal characteristics beneath the Hoggar swell, Algeria, revealed by systematic analyses of receiver functions from a single seismic station. *Geochemistry, Geophysics, Geosystems*, *11*, Q08011. https://doi.org/10.1029/2010GC003091

Liu, K. H., Gao, S. S., Silver, P. G., & Zhang, Y. K. (2003). Mantle layering across central South America. *Journal of Geophysical Research*, *108*(B11), 2510. https://doi.org/10.1029/2002JB002208

Mohamed, A. A., Gao, S. S., Elsheikh, A. A., Liu, K. H., Yu, Y., & Fat-Helbary, R. E. (2014). Seismic imaging of mantle transition zone discontinuities beneath the northern Red Sea and adjacent areas. *Geophysical Journal International*, *199*(2), 648–657. https://doi.org/10.1093/gji/ggu284

Montelli, R., Nolet, G., Dahlen, F. A., Masters, G., Engdahl, E. R., & Hung, S. (2004). Finite-frequency tomography reveals a variety of plumes in the mantle. *Science*, *303*(5656), 338–343. https://doi.org/10.1126/science. 1092485

Moucha, R., & Forte, A. M. (2011). Changes in African topography driven by mantle convection. *Nature Geoscience*, *4*(10), 707–712. https://doi.org/10.1038/ngeo1235

Mulibo, G. D., & Nyblade, A. A. (2013a). The *P* and *S* wave velocity structure of the mantle beneath eastern Africa and the African superplume anomaly. *Geochemistry, Geophysics, Geosystems*, *14*, 2696–2715. https://doi.org/10.1002/ggge.20150

Mulibo, G. D., & Nyblade, A. A. (2013b). Mantle transition zone thinning beneath eastern Africa: Evidence for a whole-mantle superplume structure. *Geophysical Research Letters*, *40*, 3562–3566. https://doi.org/10.1002/grl.50694

Nyblade, A. A., & Robinson, S. W. (1994). The African superswell. *Geophysical Research Letters*, *21*(9), 765–768. https://doi.org/10.1029/94GL00631

O'Donnell, J. P., Adams, A., Nyblade, A. A., Mulibo, G. D., & Tugume, F. (2013). The uppermost mantle shear wave velocity structure of eastern Africa from Rayleigh wave tomography: Constraints on rift evolution. *Geophysical Journal International*, *194*(2), 961–978. https://doi.org/10.1093/gji/ggt13w5

O'Donnell, J. P., Selway, K., Nyblade, A. A., Brazier, R., Tahir, N. E., & Durrheim, R. (2016). Thick lithosphere, deep crustal earthquakes and no melt: A triple challenge to understanding extension in the western branch of the East African Rift. *Geophysical Journal International*, *204*(2), 985–998. https://doi.org/10.1093/gji/ggv492

Ohtani, E., Litasov, K., Hosoya, T., Kubo, T., & Kondo, T. (2004). Water transport into the deep mantle and formation of a hydrous transition zone. *Physics of the Earth and Planetary Interiors*, *143*(1-2), 255–269. https://doi.org/10.1016/j.pepi.2003.09.015

Owens, T. J., Nyblade, A. A., Gurrola, H., & Langston, C. A. (2000). Mantle transition zone structure beneath Tanzania, East Africa. *Geophysical Research Letters*, *27*(6), 827–830. https://doi.org/10.1029/1999GL005429

Pasyanos, M. E., & Nyblade, A. A. (2007). A top to bottom lithospheric study of Africa and Arabia. *Tectonophysics*, *444*(1), 27–44. https://doi.org/10.1016/j.tecto.2007.07.008

Priestley, K., McKenzie, D., Debayle, E., & Pilidou, S. (2008). The African upper mantle and its relationship to tectonics and surface geology. *Geophysical Journal International*, *175*(3), 1108–1126. https://doi.org/10.1111/j.1365-246X.2008.03951.x

Quere, S., & Forte, A. M. (2006). Influence of past and present-day plate motions on spherical models of mantle convection: Implications for mantle plumes and hotspots. *Geophysical Journal International*, *165*(3), 1041–1057. https://doi.org/10.1111/j.1365-246X.2006.02990.x

Reed, C. A., Gao, S. S., Liu, K. H., & Yu, Y. (2016). The mantle transition zone beneath the Afar Depression and adjacent regions: Implications for mantle plumes and hydration. *Geophysical Journal International*, *205*(3), 1756–1766. https://doi.org/10.1093/gji/ggw116

Reed, C. A., Liu, K. H., Chindandali, P., Massingue, B., Mdala, H., Mutamina, D., … Gao, S. S. (2016). Passive rifting of thick lithosphere in the southern East African Rift: Evidence from mantle transition zone discontinuity topography. *Journal of Geophysical Research: Solid Earth*, *121*, 8068–8079. https://doi.org/10.1002/2016JB013131

Reed, C. A., Liu, K. H., Yu, Y., & Gao, S. S. (2017). Seismic anisotropy and mantle dynamics beneath the Malawi Rift Zone, East Africa. *Tectonics*, *36*, 1338–1351. https://doi.org/10.1002/2017TC004519

Ringwood, A. E. (1975). *Composition and petrology of the Earth's mantle* (1ed., 672 pp.). New York: McGraw-Hill.

Ringwood, A. E. (1991). Phase transformations and their bearing on the constitution and dynamics of the mantle. *Geochimica et Cosmochimica Acta*, *55*(8), 2083–2110. https://doi.org/10.1016/0016-7037(91) 90090-R

Ritsema, J., Nyblade, A. A., Owens, T. J., Langston, C. A., & VanDecar, J. C. (1998). Upper mantle seismic velocity structure beneath Tanzania, east Africa: Implications for the stability of cratonic lithosphere. *Journal of Geophysical Research*, *103*(B9), 21,201–21,213. https://doi.org/10.1029/98JB01274

Ritsema, J., van Heijst, H. J., & Woodhouse, J. H. (1999). Complex shear wave velocity structure imaged beneath Africa and Iceland. *Science*, *286*(5446), 1925–1931. https://doi.org/10.1126/science.286.5446.1925

Roberts, E. M., Stevens, N., O'Connor, P., Dirks, P., Gottfried, M. D., Clyde, W., … Hemming, S. (2012). Initiation of the western branch of the East African Rift coeval with the eastern branch. *Nature Geoscience*, *5*(4), 289–294. https://doi.org/10.1038/ngeo1432

Rychert, C. A., Hammond, J. O., Harmon, N., Kendall, J. M., Keir, D., Ebinger, C., … Stuart, G. (2012). Volcanism in the Afar Rift sustained by decompression melting with minimal plume influence. *Nature Geoscience*, *5*(6), 406–409. https://doi.org/10.1038/ngeo1455

Schmandt, B., & Humphreys, E. (2010). Complex subduction and small-scale convection revealed by body-wave tomography of the western United States upper mantle. *Earth and Planetary Science Letters*, *297*(3), 435–445. https://doi.org/10.1016/j.epsl.2010.06.047

Schubert, G., Anderson, C., & Goldman, P. (1995). Mantle plume interaction with an endothermic phase change. *Journal of Geophysical Research*, *100*(B5), 8245–8256. https://doi.org/10.1029/95JB0003

Shearer, P. M., & Masters, T. G. (1992). Global mapping of topography on the 660-km discontinuity. *Nature*, *335*(6363), 791–796.

Slack, P. D., & Davis, P. M. (1994). Attenuation and velocity of *P*-waves in the mantle beneath the East African Rift, Kenya. *Tectonophysics*, *236*(1–4), 331–358. https://doi.org/10.1016/0040-1951(94) 90183-X

Smith, W., & Wessel, P. (1990). Gridding with continuous curvature splines in tension. *Geophysics*, *55*(3), 293–305. https://doi.org/10.1190/1.1442837

Stamps, D. S., Flesch, L., Calais, E., & Ghosh, A. (2014). Current kinematics and dynamics of Africa and the East African Rift System. *Journal of Geophysical Research: Solid Earth*, *119*, 5161–5186. https://doi.org/10.1002/2013JB010717

Stamps, D. S., Iaffaldano, G., & Calais, E. (2015). Role of mantle flow in Nubia-Somalia plate divergence. *Geophysical Research Letters*, *42*, 290–296. https://doi.org/10.1002/2014GL062515

Tauzin, B., Debayle, E., & Wittlinger, G. (2008). The mantle transition zone as seen by global *Pds* phases: No clear evidence for a thin transition zone beneath hotspots. *Journal of Geophysical Research*, *113*, B08309. https://doi.org/10.1029/2007JB005364

Tauzin, B., & Ricard, Y. (2014). Seismically deduced thermodynamics phase diagrams for the mantle transition zone. *Earth and Planetary Science Letters*, *401*, 337–346. https://doi.org/10.1016/j.epsl.2014.05.039

Tschauner, O., Ma, C., Beckett, J. R., Prescher, C., Prakapenka, V. B., & Rossman, G. R. (2014). Discovery of bridgmanite, the most abundant mineral in Earth a shocked meteorite. *Science*, *346*(6213), 1100–1102. https://doi.org/10.1126/science.1259369

Vauchez, A., Dineur, F., & Rudnick, R. (2005). Microstructure, texture and seismic anisotropy of the lithospheric mantle above a mantle plume: Insights from the Labait volcano xenoliths (Tanzania). *Earth and Planetary Science Letters*, *232*(3), 295–314. https://doi.org/10.1016/j.epsl.2005.01.024

Yu, Y., Gao, S. S., Moidaki, M., Reed, C. A., & Liu, K. H. (2015). Seismic anisotropy beneath the incipient Okavango rift: Implications for rifting initiation. *Earth and Planetary Science Letters*, *430*, 1–8. https://doi.org/10.1016/j.epsl.2015.08.009

Yu, Y., Liu, K. H., Moidaki, M., Reed, C. A., & Gao, S. S. (2015). No thermal anomalies in the mantle transition zone beneath an incipient continental rift: Evidence from the first receiver function study across the Okavango Rift Zone, Botswana. *Geophysical Journal International*, *202*(2), 1407–1418. https://doi.org/10.1093/gji/ggv229